

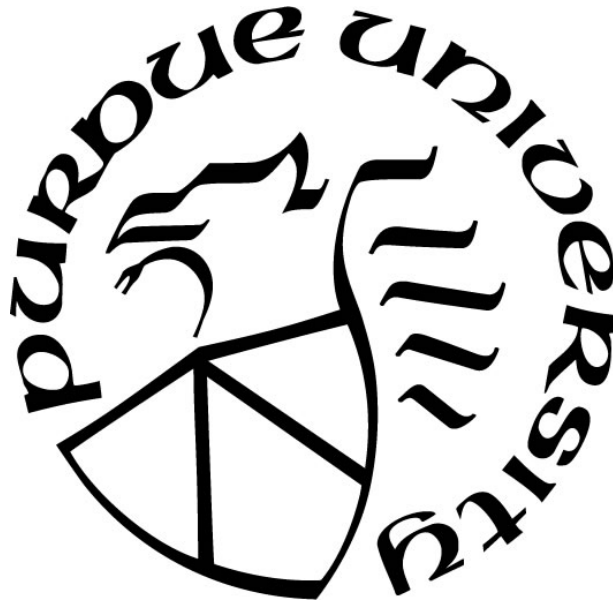
**IMPROVEMENT OF STRUCTURED LIGHT SYSTEMS USING  
COMPUTER VISION TECHNIQUES**

by  
**Yaan Zhang**

**A Thesis**

*Submitted to the Faculty of Purdue University  
In Partial Fulfillment of the Requirements for the degree of*

**Master of Science in Electrical and Computer Engineering**



Department of Electrical and Computer Engineering

Hammond, Indiana

May 2020

**THE PURDUE UNIVERSITY GRADUATE SCHOOL**  
**STATEMENT OF COMMITTEE APPROVAL**

**Dr. Lizhe Tan, Chair**

Department of Electrical and Computer Engineering

**Dr. Quamar Niyaz**

Department of Electrical and Computer Engineering

**Dr. Xiaoli Yang**

Department of Electrical and Computer Engineering

**Approved by:**

Dr. Vijay Devabhaktuni

*Dedicated to my parents Jianxing Zhang and Shuangqing Zhang*

## ACKNOWLEDGMENTS

I would like to express my gratitude to all those who helped me during the writing of this thesis. My deepest gratitude goes first and foremost to Professor Dr. Lizhe Tan, an academic advisor, for his constant encouragement and guidance. He has walked me through all the stages of the writing of this thesis. Without his consistent and illuminating instruction, this thesis could not have reached its present form. Under his guidance, I have learned much knowledge and many methods for the research.

I also owe a particular debt of gratitude to my other committee members, Dr. Quamar Niyaz and Dr. Xiaoli Yang, for their feedbacks. I would also like to thank Dr. Xinnian Guo (a visiting scholar from Huaiyin Institute of Technology, China) for his helpful discussion and suggestions. Last, my thanks would go to my beloved family for their thoughtful considerations and high confidence in me all through these years. I also owe my sincere gratitude to my friends and my classmates who gave me their help and time in listening to me and helping me work out my problems during the challenging course of the thesis.

# TABLE OF CONTENTS

LIST OF TABLES .....	7
LIST OF FIGURES .....	8
ABBREVIATIONS .....	10
ABSTRACT.....	11
1. INTRODUCTION .....	12
1.1 Motivations .....	12
1.2 Objective.....	13
1.3 Organization of Thesis.....	13
1.4 Contribution of the thesis.....	13
2. STRUCTURED LIGHT VISION SYSTEM WITH MULTI-LASER EMITTERS .....	14
2.1 Structured Light System Model.....	14
2.2 The Significance of Camera Calibration.....	14
2.2.1 Coordinate transformation.....	15
2.3 Framework of Single Camera and Multi-Laser Emitters.....	18
2.4 Calibration.....	20
2.4.1 Calculating Camera Extrinsic Parameters .....	20
2.4.2 Calculating Internal Parameters.....	21
2.4.3 Radial distortion estimation.....	22
2.4.4 Laser Plane Calibration.....	22
3. IMPROVEMENT OF THE STRUCTURED LIGHT VISION SYSTEM.....	25
3.1 Time Division Measurement.....	25
3.2 Color Division Measurement.....	28
3.3 Multi-Level Random Sample Consensus Algorithm (MLRANSAC).....	32
4. EXPERIMENT AND PROCESSING.....	38
4.1 System Calibration Results .....	39
4.2 Height Measurement and Results .....	39
4.3 3-D Point Reconstruction Results.....	45
4.4 Error Analysis and Engineering Suggestions .....	52
5. CONCLUSION.....	53

REFERENCES .....	54
PUBLICATIONS.....	56

## LIST OF TABLES

Table 3.1 Thresholds Settings.....	30
Table 4.1 Time Division Method.....	42
Table 4.2 Color Division Method.....	43
Table 4.3 Multi-level RANSAC Algorithm.....	44

## LIST OF FIGURES

Figure 2.1 Height measurement system.....	14
Figure 2.2 The relationship chat of Image coordinate and pixel coordinate. ....	16
Figure 2.3 Transformations from world coordinates to pixel coordinates.....	18
Figure 3.1 First set of pictures .....	26
Figure 3.2 Second set of pictures .....	26
Figure 3.3 Third set of pictures.....	26
Figure 3.4 Fourth set of pictures .....	27
Figure 3.5 Fifth set of pictures .....	27
Figure 3.6 The process of the time division.....	28
Figure 3.7 Histogram of measured image in RGB color space. ....	29
Figure 3.8 Results of color separation in different exposure time.....	30
Figure 3.9 The process of the color division method.....	31
Figure 3.10 The process of the MLRANSAC algorithm.....	33
Figure 3.11 First level of MLRANSAC algorithm.....	34
Figure 3.12 Second level of MLRANSAC algorithm. ....	35
Figure 3.13 The “best straight line”.....	35
Figure 3.14 Some points that cannot be decided to which laser emitters. ....	36
Figure 3.15 The distance factor. ....	36
Figure 3.16 The direction factor. ....	37
Figure 4.1 Proposed structured-light measurement system .....	38
Figure 4.2 Measurement for m1 and m2.....	40
Figure 4.3 Measurement for m3 and m4.....	41
Figure 4.4 Measurement for m5 and m6.....	42
Figure 4.5 Reconstruction resulta .....	45
Figure 4.6 3-D reconstruction of m1 using time division.....	46
Figure 4.7 3-D reconstruction of m1 using color division.....	46
Figure 4.8 3-D reconstruction of m1 using the MLRANSAC algorithm .....	46

Figure 4.9 3-D reconstruction of m2 using time division.....	47
Figure 4.10 3-D reconstruction of m2 using color division.....	47
Figure 4.11 3-D reconstruction of m2 using the MLRANSAC algorithm .....	47
Figure 4.12 3-D reconstruction of m3 using time division.....	48
Figure 4.13 3-D reconstruction of m3 color division. ....	48
Figure 4.14 3-D reconstruction of m3 MLRANSAC algorithm.....	48
Figure 4.15 3-D reconstruction of m4 using time division.....	49
Figure 4.16 3-D reconstruction of m4 using color division.....	49
Figure 4.17 3-D reconstruction of m4 MLRANSAC algorithm.....	49
Figure 4.18 3-D reconstruction of m5 using time division.....	50
Figure 4.19 3-D reconstruction of m5 using color division.....	50
Figure 4.20 3-D reconstruction of m5 MLRANSAC algorithm.....	50
Figure 4.21 3-D reconstruction of m6 using time division.....	51
Figure 4.22 3-D reconstruction of m6 using color division.....	51
Figure 4.23 3-D reconstruction of m6 MLRANSAC algorithm.....	51

## ABBREVIATIONS

MLRANSAC	Multi-Level Random Sample Consensus
3D	three-dimensional
CCD	Charge-coupled Device
RANSAC	Random Sample Consensus
SSD	Solid State Drive

## **ABSTRACT**

In this thesis work, we propose computer vision techniques for 3D reconstruction and object height measurement using a single camera and multi-laser emitters, which have an intersection on the projected image plane. Time-division and color division methods are first investigated for our structured light system. Although the color division method offers better accuracy for object height measurement, it requires the laser emitters equipped with different color lights. Furthermore, the color division method is sensitive to light exposure in the measurement environment. Next, a new multi-level random sample consensus (MLRANSAC) algorithm has been developed. The proposed MLRANSAC method not only offers high accuracy for object height measurement but also eliminates the requirement for the laser emitters with different colors. Our experiment results have validated the effectiveness of the MLRANSAC algorithm.

# 1. INTRODUCTIONS

## 1.1 Motivations

Structured light has been widely applied in computer vision applications as a three-dimension reconstruction [1]-[3]. Comparing with the passive vision method, the structured light technique can adapt to less texture and low illuminate conditions, so it has higher reliability and accuracy over short distances. The structured light techniques also contribute a lot in industries such as archaeology, agriculture, architecture, autopilot, and so on [4]-[8]. Laser emitters [1]-[3], [9]-[12] capable of emitting laser lines and projectors [11], [13]-[15] capable of posting encoded patterns are often used as light sources to utilize their geometric properties. A vision system with a light source and a camera placed at various angles provides sufficient information for a basic 3D reconstruction [16].

Since the image captured by a camera is the only source of information from the system, and to reduce the difficulty of the feature extraction, the complexity of posting patterns and laser planes is limited. A common technique prefers parallel lines [4] rather than intersections in the structured light patterns to avoid the difficulties of image processing. For example, a laser-scanned system uses one single laser line. It then reconstructs the model by moving the object along a specific orientation [8] or rotating the system along with a certain point [3], [7]. For a projector system, the binary gray-code pattern [11], [13] is widely applied, which is an accepted time-domain encode method. This method encodes each pixel as gray code by regularly posting patterns with black and white strips. Square dots are also applied as a post pattern in a projector system [14]. Using the intersections in light patterns is generally to be avoided in the structured light system; however, it can be useful for some situations, such as the object height measurement. Furthermore, computer vision algorithms can be developed to relieve the constraint of the intersections in light patterns.

This research work focuses on the structured light system with a single camera and multi-laser emitters. The motivation of the thesis is to tackle the challenging problems for the 3D object reconstruction and height measurement using the projected intersections inline patterns from a single camera and multi-laser emitters.

## **1.2 Objective**

In this research, we construct a structured light system using a single camera and multi-laser emitters and investigate as well as propose the computer vision algorithms for object measurement using the intersections inline patterns on the projected image plane. We classify our vision techniques into three methods: time-division, color division, and random sample consensus. We propose computer vision techniques and algorithms for each classified method for 3D object reconstruction and height measurement. An advanced sample consensus algorithm with multi-level detection is developed and investigated. Finally, we compare the measurement results from three developed computer vision methods and validate which way achieves the best measurement results.

## **1.3 Organization of Thesis**

The structure of this thesis paper is organized as follows. Chapter 2 introduces a structured light vision system with multi-laser emitters. In Chapter 3, three methods for improving structured light systems are described in detail. The three optimization algorithms, time-division algorithm, color division algorithm, and multi-level random sample consensus algorithm, are proposed. We then compare and analyze experimental results in Chapter 4. Finally, Chapter 5 presents the conclusion, contribution, and future work.

## **1.4 Contribution of Thesis**

This thesis has three contributions. First, we develop the relevant mathematical framework for a structured system with a single camera and multiple laser emitters. Secondly, the time division, color division, and multi-level random sample consensus (RANSAC) algorithm are proposed to measure the height of the object. Finally, by comparing the results of the three methods, it is verified that the performance of the multi-level RANSAC (MLRANSAC) algorithm offers the best measurement.

## 2. STRUCTURED LIGHT VISION SYSTEM WITH MULTI-LASER EMITTERS

### 2.1 Structured Light System Model

In this section, we will develop the mathematical framework. Figure 2.1 shows our measurement system. It consists of a high definition camera, a processing platform, and  $N$  laser transmitters with red, green, and blue color options. As shown in Figure 2.1, the world coordinate and the camera coordinate are represented by  $oxyz$  and  $o_c x_c y_c z_c$ , respectively. Note that the equation:  $z=0$  presents the horizontal plane in the world coordinate. It is assumed that the projection of the triangular plane on the plane of  $z=0$  exists and can be captured by the camera.

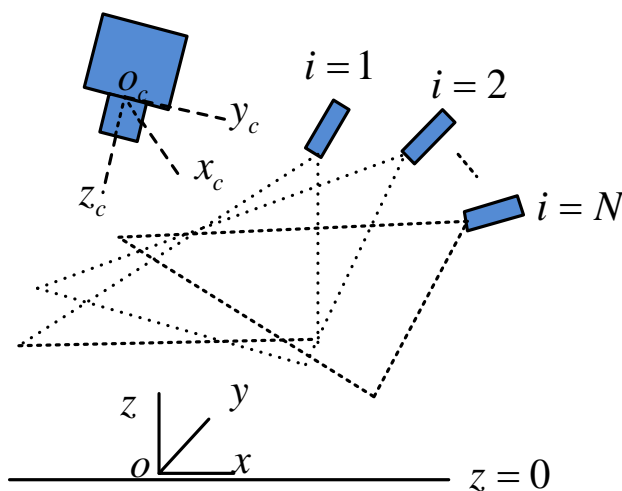


Figure 2.1 Height measurement system.

### 2.2 The Significance of Camera Calibration

In the field of machine vision, the calibration of the camera is a critical task, which determines whether the machine vision system can be positioned effectively and can calculate the target effectively. Camera calibration can be divided into two types; the first type deals with the camera's self-calibration; the second type copies with the calibration, which depends on the calibration reference object. The former is to use a camera to photograph surrounding objects. The camera parameters are obtained by digital image processing and related geometric calculations.

However, the calibration results by this method exhibit substantial errors and thus is not suitable for high-precision applications. The latter involves calculating the internal and external parameters of the camera by calibrating reference objects, imaging by the camera, and using digital image processing methods, as well as later spatial arithmetic operations. This method of calibration using the reference object has high calibration accuracy and is suitable for applications requiring high precision.

### 2.2.1 Coordinate transformation

Several coordinate systems must be introduced and are described below:

World coordinate system: the absolute coordinate system in the objective three-dimensional world is also called the world coordinate system. Because the digital camera is placed in three-dimensional space, we need the world coordinate system, which is the reference coordinate system, to describe the position of the digital camera, and use it to describe the position of any other object placed in this three-dimensional environment.  $(x, y, z)$  designates its coordinate component values.

Camera coordinate system (light center coordinate system): With the camera's optical center as the origin, the  $X$  and  $Y$  axes are respectively parallel to the  $X$  and  $Y$  axes of the image coordinate system (depicted next). The camera's optical axis is denoted by  $Z$ -axis, and its coordinate values can be expressed by  $(x_c, y_c, z_c)$ .

Image coordinate system: Taking the center of the CCD image plane as the coordinate origin, the  $X$ -axis and  $Y$ -axis are parallel to the two vertical edges of the image plane, respectively, and its coordinate values are represented by  $(x, y)$ . The image coordinate system describes the position of a pixel in an image in physical units, such as millimeters.

Pixel coordinate system: taking the vertex of the upper left corner of the CCD image plane as the origin, the  $X$  and  $Y$  axes are parallel to the  $X$  and  $Y$  axes of the image coordinate system, respectively, and its coordinate values are represented by  $(u, v)$ . The image collected by the digital camera is first formed into the form of a standard electrical signal and then converted into a digital image by analog-to-digital conversion. An image has a size of an  $M \times N$  containing  $M \times N$  elements. Each such component is called a pixel, which consists of red, green, blue color components. The pixel coordinate system is an image coordinate system in pixels. The pixel coordinate system is a two-dimensional coordinate system, which reflects the arrangement of

pixels in the CCD chip of the camera. The origin is located in the upper left corner of the image, as shown in Figure 2.2.

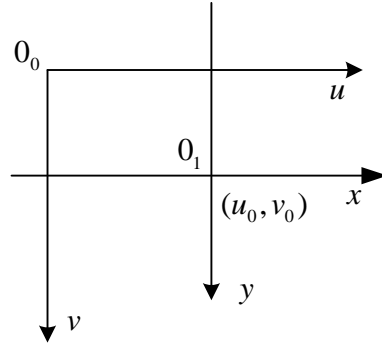


Figure 2.2 The relationship chat of Image coordinate and pixel coordinate.

The following relationships exist between the pixel coordinates and image coordinates:

$$u = \frac{x}{dx} + u_0 \quad (2.1)$$

$$v = \frac{y}{dy} + v_0 \quad (2.2)$$

If the unit in the physical coordinate system is in millimeter, then the unit of  $dx$  is: mm/pixel and the unit of  $x/dx$  is in terms of the pixels. Hence, the unit is the same as that of  $u$ . For ease of use, Equations (2.2) can be expressed in homogeneous coordinates. The matrix form is given by:

$$\begin{bmatrix} u \\ v \\ 1 \end{bmatrix} = \begin{bmatrix} 1/dx & 0 & u_0 \\ 0 & 1/dy & v_0 \\ 0 & 0 & 1 \end{bmatrix} \begin{bmatrix} x \\ y \\ 1 \end{bmatrix} \quad (2.3)$$

The relationship between the image coordinate system and camera coordinate system can be obtained as

$$\begin{cases} x = \frac{f x_c}{z_c} \\ y = \frac{f y_c}{z_c} \end{cases} \quad (2.4)$$

where  $f$  is the focal length (the distance between the image plane and the origin of the camera coordinate system). Hence, the transformation can further be expressed as:

$$z_c \begin{bmatrix} x \\ y \\ 1 \end{bmatrix} = \begin{bmatrix} f & 0 & 0 & 0 \\ 0 & f & 0 & 0 \\ 0 & 0 & 1 & 0 \end{bmatrix} \begin{bmatrix} x_c \\ y_c \\ z_c \\ 1 \end{bmatrix} = \begin{bmatrix} f & 0 & 0 \\ 0 & f & 0 \\ 0 & 0 & 1 \end{bmatrix} \begin{bmatrix} 1 & 0 & 0 & 0 \\ 0 & 1 & 0 & 0 \\ 0 & 0 & 1 & 0 \end{bmatrix} \begin{bmatrix} x_c \\ y_c \\ z_c \\ 1 \end{bmatrix} \quad (2.5)$$

The relationship between the camera coordinate system and the world coordinate system can be established using the homogeneous expression is:

$$\begin{bmatrix} x_c \\ y_c \\ z_c \\ 1 \end{bmatrix} = \begin{bmatrix} R & t \\ 0 & 1 \end{bmatrix} \begin{bmatrix} x \\ y \\ z \\ 1 \end{bmatrix} \quad (2.6)$$

where  $R$  is the 3x3 rotation matrix and  $t$  is the translation vector.  $R$  and  $t$  are independent of the internal parameters of camera, so these two parameters are called the extrinsic parameters of the camera, which denotes the relation between the two coordinate origins.

If the transformation from camera coordinate to image coordinate and the transformation from image coordinates to pixel coordinate are combined together, the following equation can be obtained:

$$z_c \begin{bmatrix} u \\ v \\ 1 \end{bmatrix} = z_c \begin{bmatrix} \frac{1}{dx} & 0 & u_0 \\ 0 & \frac{1}{dy} & v_0 \\ 0 & 0 & 1 \end{bmatrix} \begin{bmatrix} x \\ y \\ 1 \end{bmatrix} = \begin{bmatrix} \frac{1}{dx} & 0 & u_0 \\ 0 & \frac{1}{dy} & v_0 \\ 0 & 0 & 1 \end{bmatrix} \begin{bmatrix} f & 0 & 0 & 0 \\ 0 & f & 0 & 0 \\ 0 & 0 & 1 & 0 \end{bmatrix} \begin{bmatrix} x_c \\ y_c \\ z_c \\ 1 \end{bmatrix} \quad (2.7)$$

Three transformations consist the imaging model of the camera. The complete coordinate transformations are shown in Figure 2.3.

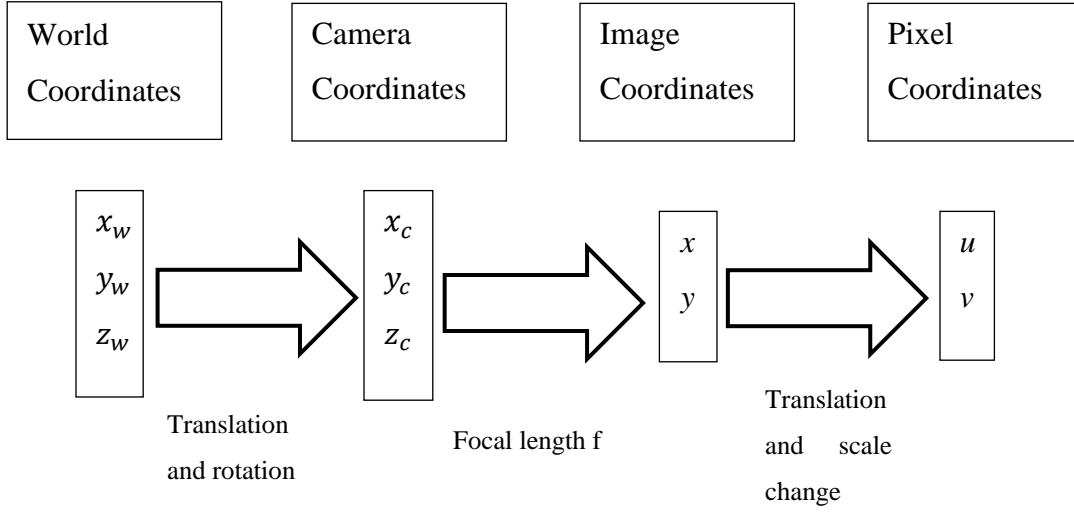


Figure 2.3 Transformations from world coordinates to pixel coordinates.

### 2.3 Framework of Single Camera and Multi-Laser Emitters

We first establish our system notations. A camera pinhole model is employed, and its perspective projection is given below:

$$X_c = z_c A^{-1} \bar{I}_p \quad (2.8)$$

$$\bar{X}_c = \begin{bmatrix} R & t \\ 0 & 1 \end{bmatrix} \bar{X} \quad (2.9)$$

For convenience, the following definitions are adopted:

$X = (x \ y \ z)^T$  - a point in the world coordinate

$\bar{X} = (x \ y \ z \ 1)^T$  - homogeneous form of  $X$

$X_c = (x_c \ y_c \ z_c)^T$  - a point in the camera coordinate

$\bar{X}_c = (x_c \ y_c \ z_c \ 1)^T$  - homogeneous form of  $X_c$

$I_p = (u \ v)^T$  - a point in the image pixel coordinate

$\bar{I}_p = (u \ v \ 1)^T$  : homogeneous form of  $I_p$

Note that  $A^{-1}$  is the inverse of intrinsic matrix  $A$ , which is defined below:

$$A = \begin{bmatrix} \alpha & c & u_0 \\ 0 & \beta & v_0 \\ 0 & 0 & 1 \end{bmatrix} \quad (2.10)$$

where  $\alpha$  and  $\beta$  are the projection of the effective focal length in  $x$ - and  $y$ - axes.  $u_0$  and  $v_0$  are the image intersection coordinates between the image plane and optical axis.  $c$  is the skewness in terms of two image axes.  $[R \ t] = [r_1 \ r_2 \ r_3 \ t]$  designates the rotation and translation between the world coordinate and camera coordinate.

Let a characteristic point  $j$  on the triangular plane  $i$  formed by the  $i$ th laser emitter be:

$$\bar{X}_{cL}(i, j) = (x_{cL}(i, j) \ y_{cL}(i, j) \ z_{cL}(i, j) \ 1)^T \quad (2.11)$$

and the  $i$ th plane is denoted by

$$\pi_i = (a_i \ b_i \ c_i \ -1)^T \quad (2.12)$$

Then it leads to the following:

$$X_{cL}(i, j) / z_c(i, j) = A^{-1} \bar{I}_p(i, j) \quad (2.13)$$

$$\pi_i \bar{X}_{cL}(i, j) = 0, \quad j = 1, 2, \dots, J \quad (2.14)$$

Given projected points  $\bar{I}_p(i, j)$  and (2.13), we can obtain

$$X_{cL}(i, j) / z_{cL}(i, j) = [x_{cL}(i, j) / z_{cL}(i, j) \ y_{cL}(i, j) / z_{cL}(i, j) \ 1] \quad (2.15)$$

Given the calibrated triangular plane  $i$ , and (2.14), we finally can yield

$$z_{cL}(i, j) = 1 / (a_i x_{cL}(i, j) / z_{cL}(i, j) + b_i y_{cL}(i, j) / z_{cL}(i, j) + c_i) \quad (2.16)$$

After applying Equation (2.8),  $X_c(i, j) = X_{cL}(i, j)$  can be obtained. Finally, we achieve

$$\bar{X}(i, j) = \begin{bmatrix} R & t \\ 0 & 1 \end{bmatrix}^{-1} \bar{X}_c(i, j) \quad (2.17)$$

It must be noted that the reconstructed points of  $X_c(i, j)$  in the camera model are unique since the camera is installed at the fixed location while the reconstructed points of  $X(i, j)$  in the world coordinate depend on the checkerboard orientation, that is,  $R$  and  $t$ .

With the calibration information of extrinsic and intrinsic matrices, and the all the calibrated triangular planes, we can develop the time division, color division, and random sample consensus (RANSAC) method to conduct 3-D reconstruction.

## 2.4 Calibration

The camera is calibrated using Zhang's method [18], where the augmented 2D and 3D points in the world coordinate are denoted by  $\tilde{m} = (u \ v \ 1)^T$ ,  $M = (x \ y \ z \ 1)^T$ , respectively. With a pinhole camera model, a relationship between a 3D point and its image project is given by

$$s\tilde{m} = A [R \ t] \ M = A [r_1 \ r_2 \ r_3 \ t] \ M \quad (2.18)$$

Using  $z = 0$  in the model plane (floor plane), (2.18) becomes

$$s\tilde{m} = A [r_1 \ r_2 \ t] \ \tilde{M} \quad (2.19)$$

where  $S$  is a scale factor and  $\tilde{M} = (x \ y \ 1)^T$ .

### 2.4.1 Calculating Camera Extrinsic Parameters

Let  $s\tilde{m} = H\tilde{M}$  with  $H = A[r_1 \ r_2 \ t]$ , then

$$z_c \begin{bmatrix} u \\ v \\ 1 \end{bmatrix} = H \cdot \begin{bmatrix} x \\ y \\ 1 \end{bmatrix} \quad (2.20)$$

$$H = [h_1 \ h_2 \ h_3] \quad (2.21)$$

Let  $H = [h_1 h_2 h_3] = \lambda A[r_1 r_2 t]$ , where  $\lambda$  is an arbitrary scaler. According to the properties of orthogonal matrices [18], it is easy to get:

$$\begin{aligned} h_1^T A^{-T} A^{-1} h_2 &= 0 \\ h_1^T A^{-T} A^{-1} h_1 &= h_2^T A^{-T} A^{-1} h_2 \end{aligned} \quad (2.22)$$

Then, the following terms can be calculated:

$$r_1 = \lambda A^{-1} h_1 \quad r_2 = \lambda A^{-1} h_2 \quad r_3 = r_1 \times r_2 \quad t = \lambda A^{-1} h_3 \quad (2.23)$$

$$\lambda = \frac{1}{\|A^{-1} h_1\|} = \frac{1}{\|A^{-1} h_2\|} \quad (2.24)$$

Notice that  $H$  has 8 unknowns, at least 8 equations are required. Each pair of points can provide two equations, so at least four pairs of points are needed to solve for  $H$ .

## 2.4.2 Calculating Internal Parameters

As  $r_1$  and  $r_2$  are orthogonal, and  $\|r_1\| = \|r_2\| = 1$ , the following constraints can be obtained:

$$\begin{cases} h_1^T A^{-T} A^{-1} h_2 = 0 \\ h_1^T A^{-T} A^{-1} h_1 = h_2^T A^{-T} A^{-1} h_2 = 1 \end{cases} \quad (2.25)$$

Define:

$$\begin{aligned} B = A^{-T} A^{-1} &= \begin{bmatrix} B_{11} & B_{12} & B_{13} \\ B_{12} & B_{22} & B_{23} \\ B_{13} & B_{23} & B_{33} \end{bmatrix} \\ &= \begin{bmatrix} \frac{1}{\alpha^2} & -\frac{\gamma}{\alpha^2 \beta} & \frac{v_0 \gamma - u_0 \beta}{\alpha^2 \beta} \\ -\frac{\gamma}{\alpha^2 \beta} & \frac{\gamma^2}{\alpha^2 \beta^2} + \frac{1}{\beta^2} & -\frac{\gamma(v_0 \gamma - u_0 \beta)}{\alpha^2 \beta^2} - \frac{v_0^2}{\beta^2} \\ \frac{v_0 \gamma - u_0 \beta}{\alpha^2 \beta} & -\frac{\gamma(v_0 \gamma - u_0 \beta)}{\alpha^2 \beta^2} - \frac{v_0^2}{\beta^2} & \frac{(v_0 \gamma - u_0 \beta)^2}{\alpha^2 \beta^2} + \frac{v_0^2}{\beta^2} + 1 \end{bmatrix} \end{aligned} \quad (2.26)$$

It can be seen that matrix  $B$  is a symmetric matrix with only six valid elements. Define vector  $b$  as

$$b = [B_{11}, B_{12}, B_{22}, B_{13}, B_{23}, B_{33}]^T \quad (2.27)$$

$B$  is composed of  $A$  matrix. Therefore, it meets the following equations:

$$h_i^T B h_j = v_{ij}^T b \quad (2.28)$$

$$\mathbf{v}_{ij} = [h_{i1} h_{j1}, h_{i1} h_{j2} + h_{i2} h_{j1}, h_{i2} h_{j2}, h_{i3} h_{j1} + h_{i1} h_{j3}, h_{i3} h_{j2} + h_{i2} h_{j3}, h_{i3} h_{j3}]^T \quad (2.29)$$

Then, the following formula can be derived:

$$\begin{bmatrix} v_{12}^T \\ (v_{11} - v_{22})^T \end{bmatrix} b = 0 \quad (2.30)$$

Since  $B$  has 6 unknowns. The dimension of bracket in (2.30) is 2x6. Thus, three images are required so that we can stack the bracket in (2.30) up to a dimension of 6x6 in order to get the unique solution of  $b$ . Then, the camera intrinsic reference matrix  $A$  can be obtained by using Cholesky decomposition algorithm to decompose matrix  $B$ .

### 2.4.3 Radial distortion estimation

We focus on the most influential radial distortion calibration proposed by Zhang's calibration method [18]. The mathematical expressions are given by:

$$\begin{aligned}\hat{x} &= x + x \left[ k_1 (x^2 + y^2) + k_2 (x^2 + y^2)^2 \right] \\ \hat{y} &= y + y \left[ k_1 (x^2 + y^2) + k_2 (x^2 + y^2)^2 \right]\end{aligned}\quad (2.31)$$

where  $(x, y)$  is the ideal undistorted image coordinate.  $(\hat{x}, \hat{y})$  is the image coordinate after the actual distortion.  $k_1$  and  $k_2$  are the distortion parameters of the first two orders. Since the center of the radial distortion and the center of the camera are in the same position, the following equations can be obtained:

$$\begin{aligned}\hat{u} &= \mu_0 + \alpha \hat{x} + \gamma \hat{y} \\ \hat{v} &= \nu_0 + \beta \hat{y}\end{aligned}\quad (2.32)$$

Assuming that  $\gamma = 0$ , the following equations can be obtained:

$$\begin{aligned}\hat{u} &= u + (u - u_0) \left[ k_1 (x^2 + y^2) + k_2 (x^2 + y^2)^2 \right] \\ \hat{v} &= v + (v - v_0) \left[ k_1 (x^2 + y^2) + k_2 (x^2 + y^2)^2 \right]\end{aligned}\quad (2.33)$$

where  $(u, v)$  is the ideal undistorted pixel coordinate, and  $(\hat{u}, \hat{v})$  is the pixel coordinate after the actual distortion.  $(u_0, v_0)$  represents the principal point.

After transferring the above equations into a matrix form, it leads to:

$$\begin{bmatrix} (u - u_0)(x^2 + y^2) & (u - u_0)(x^2 + y^2)^2 \\ (v - v_0)(x^2 + y^2) & (v - v_0)(x^2 + y^2)^2 \end{bmatrix} \begin{bmatrix} k_1 \\ k_2 \end{bmatrix} = \begin{bmatrix} \hat{u} - u \\ \hat{v} - v \end{bmatrix}\quad (2.34)$$

It can be simplified as:  $Dk = d$ . So, distortion parameter  $k$  can be calculated as:

$$k = [k_1 k_2]^T = (D^T D)^{-1} D^T d \quad (2.35)$$

### 2.4.4 Laser Plane Calibration

Each triangular plane  $\pi_i = (a_i \ b_i \ c_i \ -1)$  required in (2.14) for  $i = 1, 2, \dots, N$  is calibrated independently. As shown in Figure 2.1, let the model plane  $z = 0$  in the world

coordinate be  $(0 \ 0 \ 1 \ 0)^T$  and  $(x_i \ y_i \ z_i)$  be the characteristic point on the model plane from the  $i$ th triangular laser plane. In the world coordinate, we can get:

$$\begin{bmatrix} 0 \\ 0 \\ 1 \\ 0 \end{bmatrix}^T \begin{bmatrix} x_i \\ y_i \\ z_i \\ 1 \end{bmatrix} = 0 \quad (2.36)$$

Note that the relation of point  $(x_i \ y_i \ z_i)$  in the world coordinate and corresponding point in  $(x_{ci} \ y_{ci} \ z_{ci})$  in the camera coordinate can be expressed as :

$$\begin{bmatrix} R & t \\ 0 & 1 \end{bmatrix} \begin{bmatrix} x_i \\ y_i \\ z_i \\ 1 \end{bmatrix} = \begin{bmatrix} x_{ci} \\ y_{ci} \\ z_{ci} \\ 1 \end{bmatrix} \quad (2.37)$$

where  $R$  and  $t$  are obtained in the process of camera calibration for the specific checkerboard orientation.

Then we derive (2.38) from (2.36), (2.37) as follows.

$$\begin{bmatrix} 0 \\ 0 \\ 1 \\ 0 \end{bmatrix}^T \begin{bmatrix} R & t \\ 0 & 1 \end{bmatrix}^{-1} \begin{bmatrix} x_{ci} \\ y_{ci} \\ z_{ci} \\ 1 \end{bmatrix} = 0 \quad (2.38)$$

Using the definition in (2.36), we can translate the model plane in the world coordinate to the camera coordinate as

$$\pi_i^T = \begin{bmatrix} 0 \\ 0 \\ 1 \\ 0 \end{bmatrix}^T \begin{bmatrix} R & t \\ 0 & 1 \end{bmatrix}^{-1} \quad (2.39)$$

Taking the transpose of (2.39) leads to

$$\pi_i = \begin{bmatrix} R & t \\ 0 & 1 \end{bmatrix}^{-T} \begin{bmatrix} 0 \\ 0 \\ 1 \\ 0 \end{bmatrix} = [A \ B \ C \ D]^T \quad (2.40)$$

As a matter of fact, the projected  $J$  image points  $X_c(i, j)$  in terms of the camera coordinate must be on the model plane of the checkerboard during calibration, that is,

$$\pi_i^T X_c(i, j) = 0 \text{ for } j = 1, 2, \dots, J \quad (2.41)$$

This is equivalent to

$$\begin{aligned} z_c(i, j)[Ax_c(i, j)/z_c(i, j) + By_c(i, j)/z_c(i, j) + C] = -D \\ \text{for } j = 1, 2, \dots, J \end{aligned} \quad (2.42)$$

Note that  $x_c(i, j)/z_c(i, j)$  and  $y_c(i, j)/z_c(i, j)$  in (2.42) can be obtained using the projected pixel points, that is,

$$X_c(i, j)/z_c(i, j) = A^{-1}\bar{I}_p(i, j) \text{ for } j = 1, 2, \dots, J \quad (2.43)$$

Then we can compute  $z_c(i, j)$  in the camera coordinate via (2.42). Finally, we can achieve characteristic points as follows.

$$X_{cL}(i, j) = X_c(i, j) = z_c(i, j)A^{-1}\bar{I}_p(i, j) \quad (2.44)$$

Since the characteristic points are now known on for solving  $\pi_i = (a_i \ b_i \ c_i \ -1)$ , that is,

$$\pi_i \bar{X}_{cL}(i, j) = 0, \ j = 1, 2, \dots, J \quad (2.45)$$

and using  $M$  trials for different checkerboard orientation with its corresponding model plane at  $z_k = 0$ , it leads to the following conditions:

$$\pi_i \bar{X}_{cL}(i, j, k) = 0, \ j = 1, 2, \dots, J, \ k = 1, 2, \dots, M \quad (2.46)$$

Finally, the least squares method can be applied to find the solution for triangular plane  $i$ , that is,

$$\pi_i = (a_i \ b_i \ c_i \ -1).$$

### 3. IMPROVEMENT OF THE STRUCTURED LIGHT VISION SYSTEM

If a single camera shot is adopted and its image projection from the laser emitters has intersection, then the intersection points are difficult to be classified for measurement. The time-division, color division, and multi-level random sample consensus algorithm (MLRANSC) are proposed for applications.

#### 3.1 Time Division Measurement

For the time division method, the laser emitters are operated sequentially at different times; that is, only one laser emitter can be turned on to hit on the surface of the measured object. This method is time-consuming.

With the camera calibration and determination of each laser plane equation, we then extract the feature points corresponding to the projected image on the object and substitute the obtained feature points into the system model, the 3D information for these line feature points can be calculated. Repeating this process for each laser emitter and composing the results from all the measurements, a 3-D reconstruction can be achieved. To obtain camera calibration, we select 15 different checkerboard images to obtain the intrinsic and extrinsic parameters of the camera. These 15 images are divided into five sets of images with three images in one set corresponding to one checkerboard orientation. Figure 3.1-3.5 show the images with projections by laser emitter  $i$  from each set used for determining a laser plane equation.

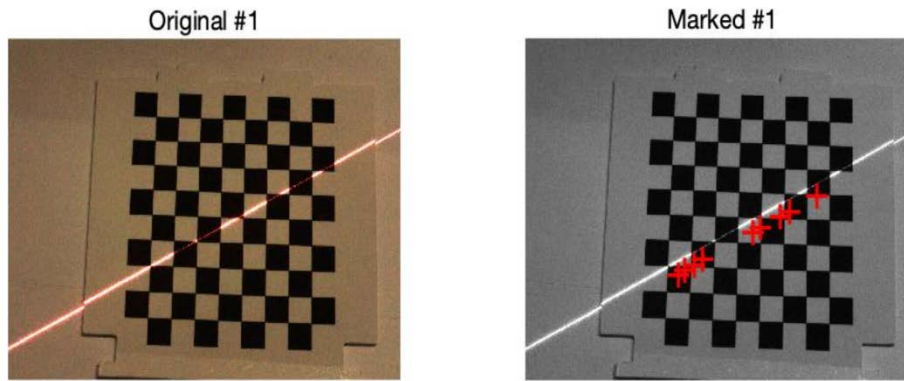


Figure 3.1 First set of pictures

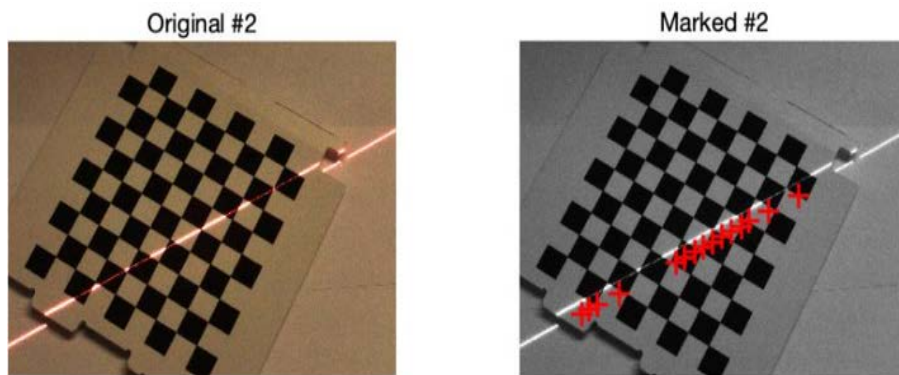


Figure 3.2 Second set of pictures

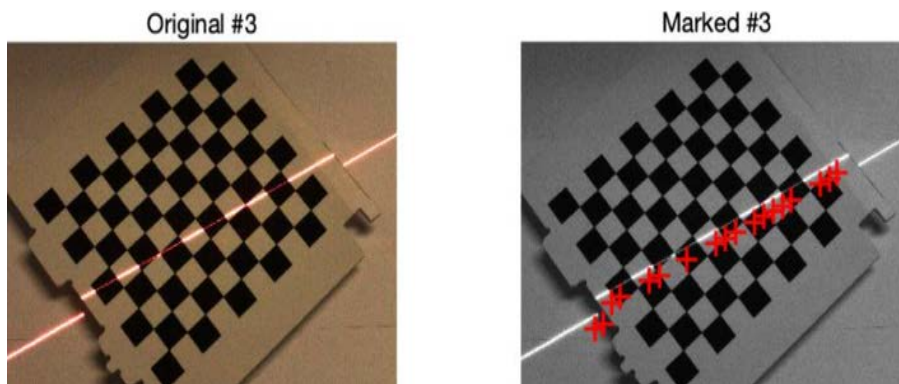


Figure 3.3 Third set of pictures

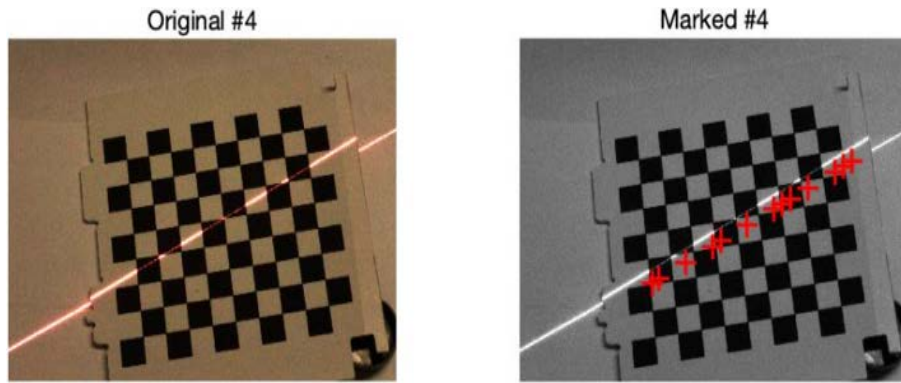


Figure 3.4 Fourth set of pictures

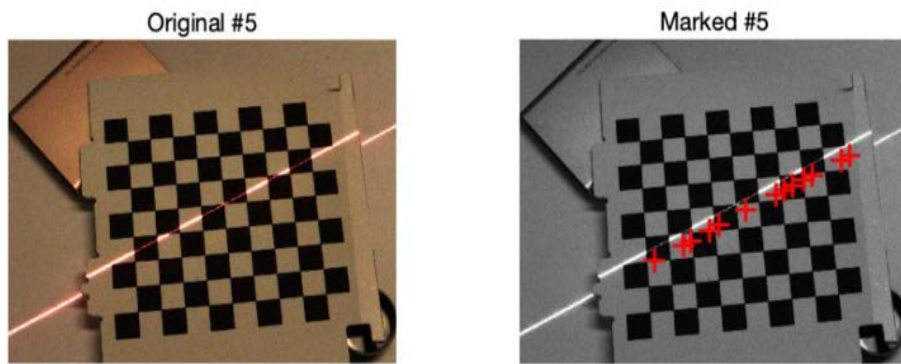


Figure 3.5 Fifth set of pictures

Figure 3.6 shows a block diagram of the process for the time division.

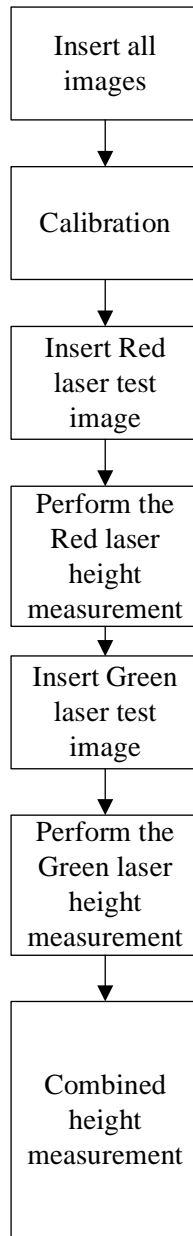


Figure 3.6 The process of the time division

### 3.2 Color Division Measurement

The color division method is developed. By setting laser emitters with different colors, the laser planes are labeled physically. Therefore, we can separate the ambiguous intersection points by processing the corresponding color plane information in the captured image. The color

threshold algorithm can further be applied to separate the color components from the laser emitter and the background color components to reduce the interference.

Figure 3.7 depicts the histograms of the measured in the RGB color space picture with turning on the red, green, and blue laser emitters simultaneously. As shown in Figure 3.7, the projected pixels from the laser emitters are near the value of 255. A pixel is identified for a certain color plane when its component value in that plane is high while the component values in the other color planes are relatively low. The color threshold algorithm can be set as follows:

$$L_i = \begin{cases} 1 & Th_{low} \leq p_i \leq Th_{high}, p_j \leq Th'_{high}, p_k \leq Th''_{high}, i \neq j \neq k \\ 0 & elsewhere \end{cases} \quad (3.1)$$

where  $L_i$  is the binary matrix for a single laser with color  $i$ .  $p_i$ ,  $p_j$  and  $p_k$  represent pixels of different color spaces.  $Th_{low}$  and  $Th_{high}$  are thresholds for color  $i$  while  $Th'_{high}$  and  $Th''_{high}$  are the threshold values for eliminating the interference caused by the other color plane components. To optimize the color separating result, red, green and blue laser emitters are utilized to match the RGB color space in our work. Table 3.1 lists threshold values for separating the color planes.

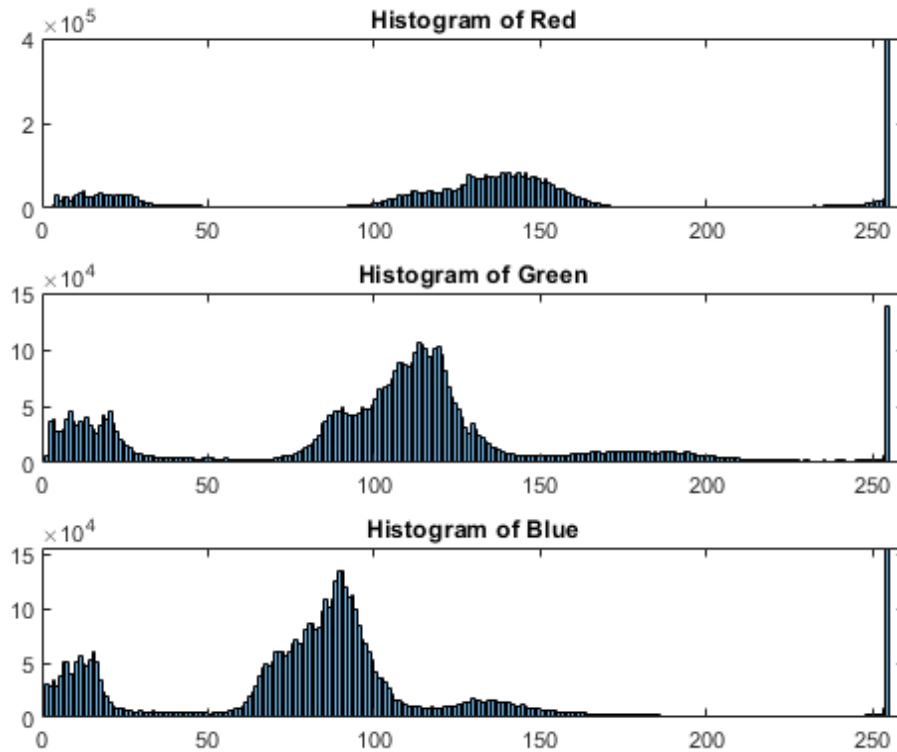


Figure 3.7 Histogram of measured image in RGB color space.

Table 3.1 Threshold values

Red laser: $250 \leq R \leq 255, G \leq 170, B \leq 170$ ;
Green laser: $230 \leq G \leq 255, B \leq 220, R \leq 220$ ;
Blue laser: $230 \leq B \leq 255, G \leq 220, R \leq 220$ ;
where, R, G and B refer to red, green, blue pixel values, respectively

As shown in Figure 3.8, the color separation based on thresholds leads to worse results when the higher exposure time of the camera is applied since parts of pixels which do not belong to lasers reach the maximum value. It affects the performance with thresholds on high exposure time pictures. It is noted that the color division method is sensitive to luminance.

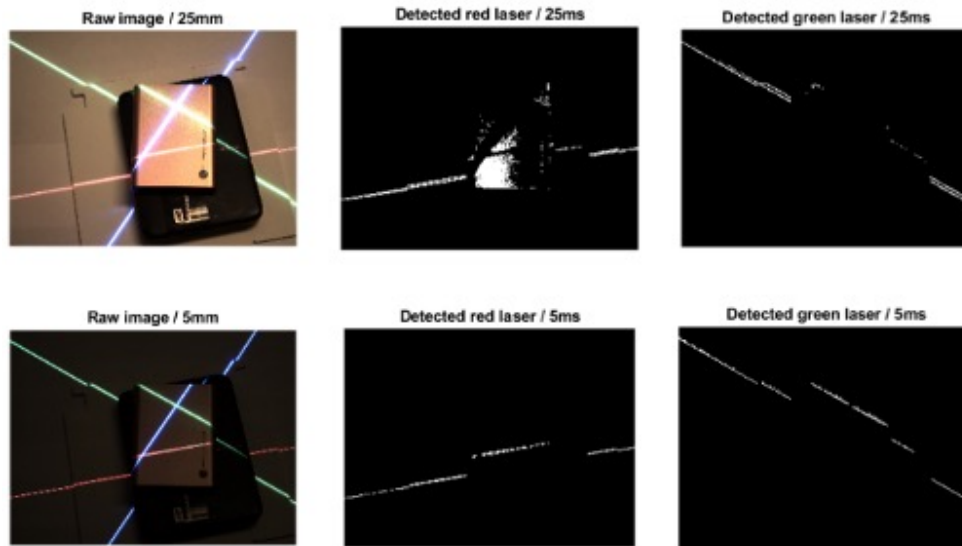


Figure 3.8 Results of color separation in different exposure time.

Figure 3.9 shows a block diagram of the process of the color division method.

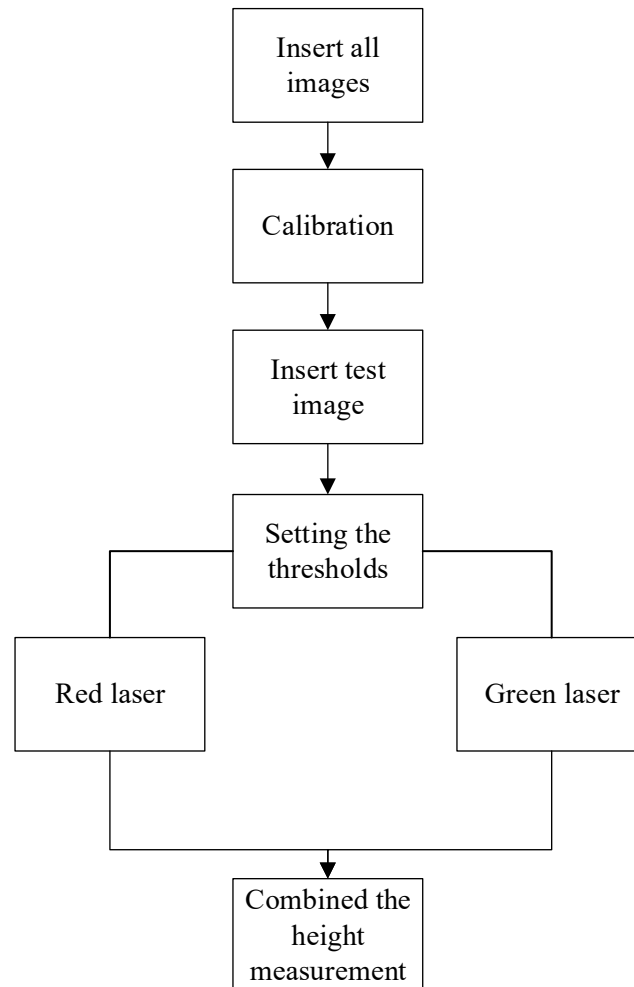


Figure 3.9 The process of the color division method.

This approach is effective, but it requires different color laser emitters. Besides, the color division method is sensitive to luminance, since with stronger luminance, parts of pixels which do not belong to lasers reach the higher value, even the maximum value. It affects the performance of the color threshold algorithm. To tackle this problem, the exposure time needs to be reduced before measurement.

### 3.3 Multi-Level Random Sample Consensus Algorithm (MLRANSAC)

In this method, we first add an additional step in the calibration stage. The points projected from the  $i$ th laser emitter on the horizontally placed checkerboard are extracted. The least squares algorithm is applied to find its linear model,  $\omega_i = (\lambda_1(i) \ \lambda_2(i) \ \lambda_0(i))^T$  corresponding to the plane  $\omega_i(u(j) \ v(j) \ 1)^T = 0$ . During the measurement stage at level 1,  $K$  points are randomly selected from the extracted point set. We compute  $K$  trial linear equations as following:

$$\bar{\lambda}_0(k) = -(\lambda_1(i)u_k + \lambda_2(i)v_k), \quad k = 1, 2, \dots, K \quad (3.2)$$

Then we use a maximum allowable distance  $d$  to determine the number of points within allowable distance  $d$ . The selected line equation is the one consisting of the maximum number of points, that is,

$$\omega_i = (\lambda_1(i) \ \lambda_2(i) \ \lambda_0(i))^T, \quad i = 1, 2, \dots, N \quad (3.3)$$

Figure 3.10 shows a block diagram of the process of the MLRANSAC algorithm.

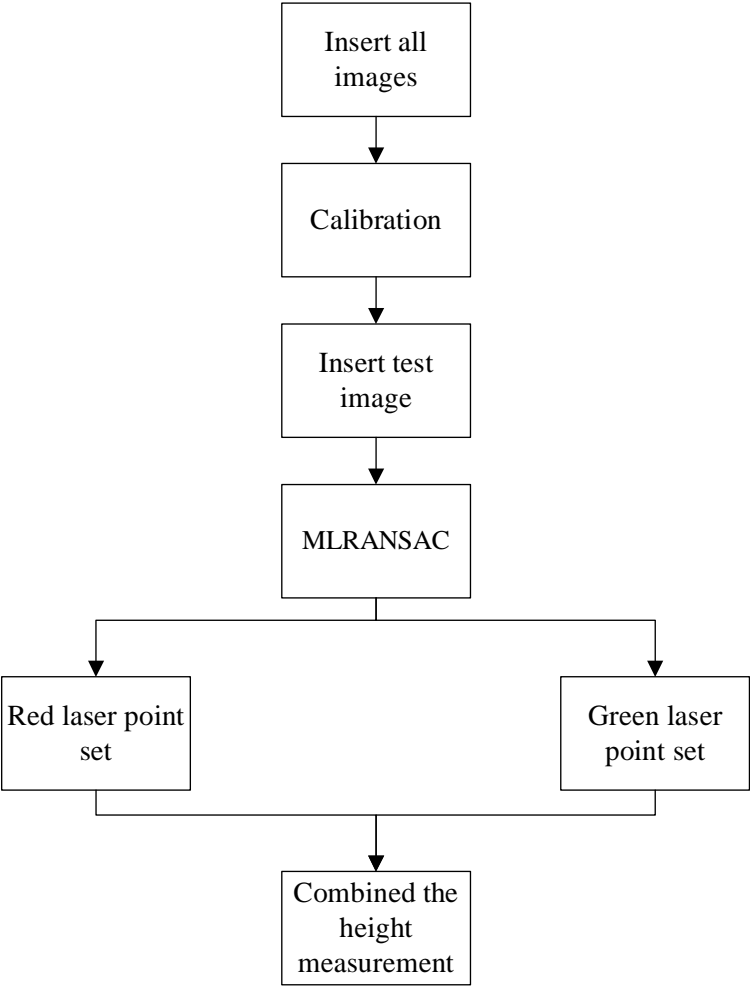


Figure 3.10 The process of the MLRANSAC algorithm.

Figure 3.11 depicts the scenario for case of  $N = 2$ .

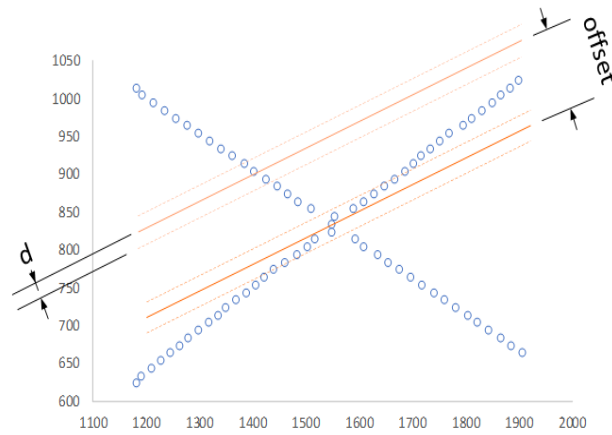


Figure 3.11 First level of MLRANSAC.

Next, we start to use Equation (3.3) as “the best straight line” representing the intersection of laser emitter  $i$ . We randomly choose two sample points from  $K$  points set to re-compute a straight line. With the obtained straight line, all extracted points are tested as follows. If the distance from a test point to the straight line is less than  $d$ , then the test point is considered on the intersection of the laser and added to the point set of the laser plane. When the cardinality of the laser plane point set corresponding to the straight line is greater than that of “the best straight line” that is, the angle between the straight line and the initial straight line in (3.3) within a threshold. Then the “best straight line” will be replaced by the current one. Iterating  $K$  times this way, the final projected line equation is obtained. Repeating this process  $N$ , we achieve final  $N$  projected linear equations as well as  $N$  sets of the projected pixel points. Figures 3.12-3.13 show the case of  $N = 2$ .

Finally, there are still some points that cannot be determined to which laser emitter they belong to (see Figure 3.14). The distance factor and direction factor at level 3 are used. The distance factor is defined as a distance ratio ( $d_1 / d_2$ ) of the undecided point from a test laser (red) intersection over the other laser (green) intersection. If the distance factor is less than a threshold, then the undecided point will be classified to this test laser point set (red). Figure 3.15 describes for the case of  $N = 2$ .

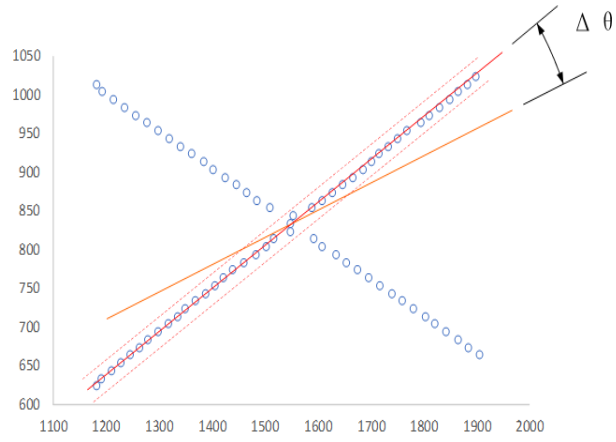


Figure 3.12 Second level of MLRANSAC.

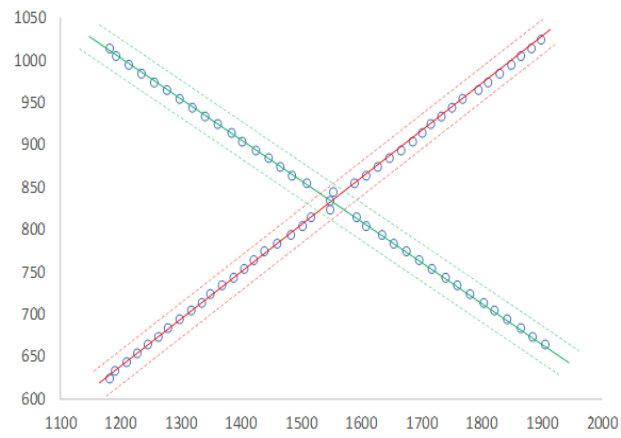


Figure 3.13 The “best straight line”.

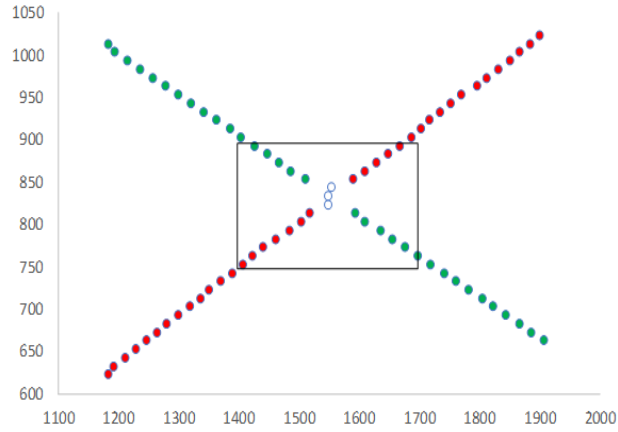


Figure 3.14 Some points that cannot be decided to which laser emitters.

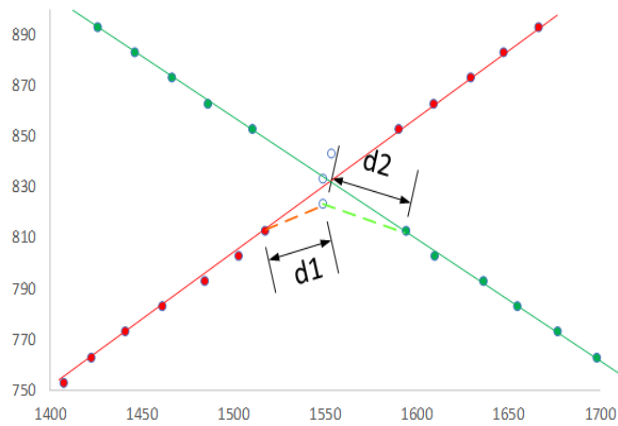


Figure 3.15 The distance factor.

The direction factor is defined as a slope ratio of the slope between the undecided point and the nearest point in the test laser point set over the final direction of the projected line. The undecided point belongs to the test laser point set if the direction factor is closer to one among the other laser point sets, as shown in Figure 3.16 for the case of  $N = 2$ .

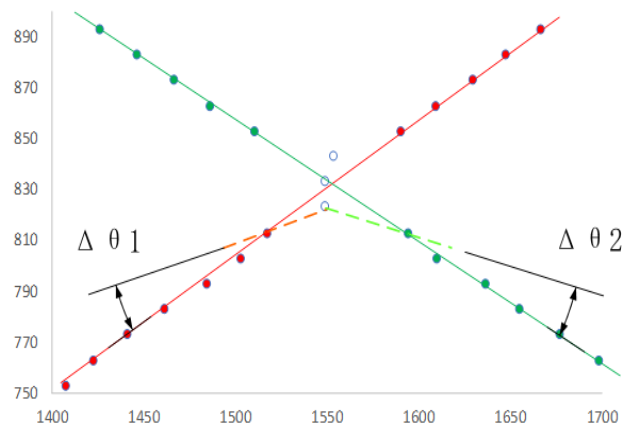


Figure 3.16 The direction factor.

## 4. EXPERIMENT AND PROCESSING

The proposed measurement system consists of a high definition camera (Basler acA2500-14gc GigE camera with ON Semiconductor MT9P031 CMOS sensor, 14 frames per second, 5MP resolution), a processing platform, checkerboard with 9\*12 squares, laser transmitters with red, green, and blue color options. To validate our proposed algorithms, two laser emitters with color options are used. In the experiment, the captured image was taken out after one photo was taken, and image processing and measurement were performed with MATLAB. Figure 4.1 depicts our system setup for measurement.

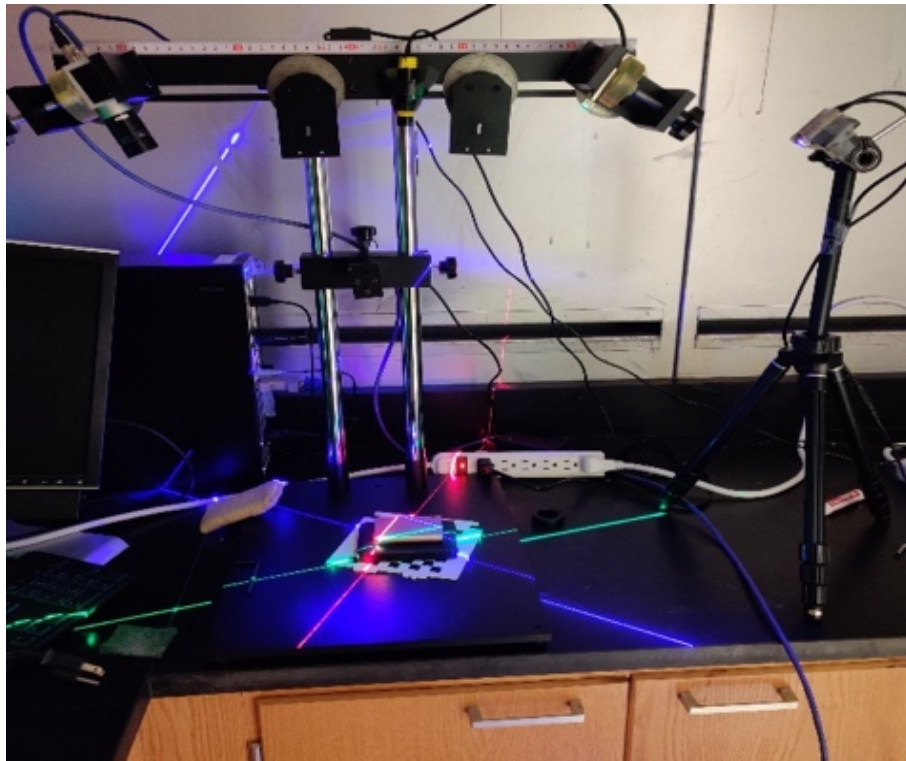


Figure 4.1 Proposed structured-light measurement system

To eliminate random error caused by multiple experiments, we used red and blue lasers in a single experiment and used grayscale images as the input of time division, color division, and MLRASAC algorithm.

## 4.1 System Calibration Results

With the Camera Calibration toolbox in MATLAB [17], the intrinsic matrix  $A$  for the camera and extrinsic parameters  $[R \ t]$  are determined. The calibrated results are listed in (4.1).

$$\begin{aligned}
 A &= \begin{bmatrix} 7.603902 \times 10^3 & 0 & 1.337963 \times 10^3 \\ 0 & 7.585635 \times 10^3 & 0.666364 \times 10^3 \\ 0 & 0 & 1 \end{bmatrix} \\
 R &= \begin{bmatrix} -0.030498 & -0.999530 & -0.003148 \\ 0.939477 & -0.029741 & 0.341319 \\ -0.341252 & 0.007452 & 0.939942 \end{bmatrix} \\
 t &= \begin{bmatrix} 0.524791 \times 10^2 \\ -0.149804 \times 10^2 \\ 5.953130 \times 10^2 \end{bmatrix}
 \end{aligned} \tag{4.1}$$

Using the checkerboard images from the sequential laser emitter projections, we achieved two planes as below:

$$\pi_1 = \begin{bmatrix} -1.895727 \times 10^{-3} \\ -3.302647 \times 10^{-3} \\ 1.924332 \times 10^{-3} \end{bmatrix} \quad \pi_2 = \begin{bmatrix} 1.424982 \times 10^{-3} \\ -1.947035 \times 10^{-3} \\ 1.800564 \times 10^{-3} \end{bmatrix} \tag{4.2}$$

## 4.2 Height Measurement and Results

Figures 4.2-4.4 display the objects for height measurements using our structured light vision system. During the measurement, we placed the object on the operating table to obtain six groups of object images, each group containing three pictures. When we used time division for height measurement, we selected images with a single laser (Figures 4.2-4.4 a and b). When using color division and MLRANSAC algorithm for height measurement, we used the images from two laser emitters as shown in Figures 4.2-4.4 c. The objects represented by m1 and m2 are Samsung SSDs, and the objects represented by m3 and m4 are western SSDs. m5 and m6 are measured by stacking Samsung SSD and Western SSD. Tables 4.1-4.3 list our height measurement results from all three methods.

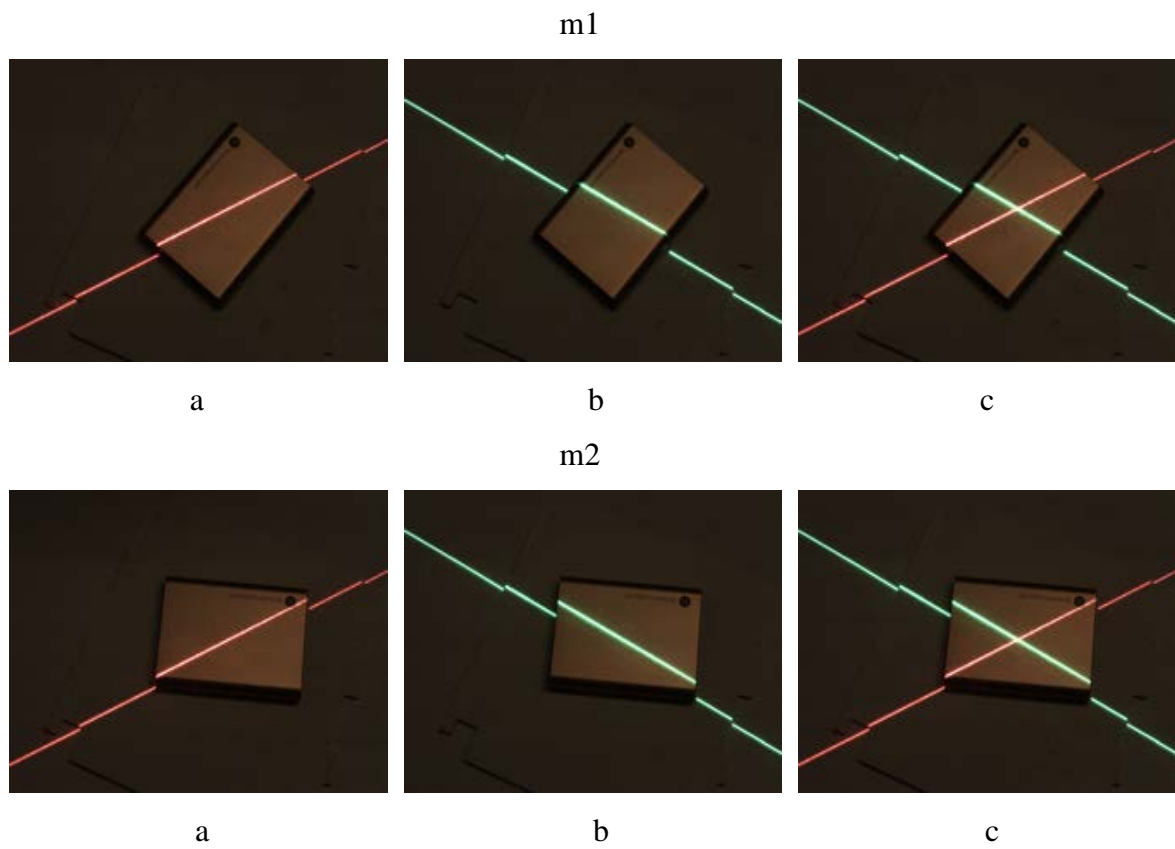
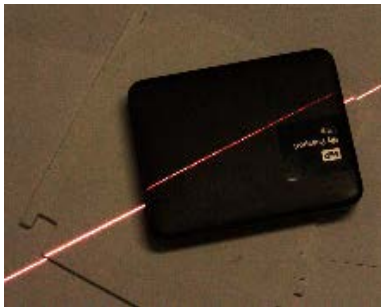
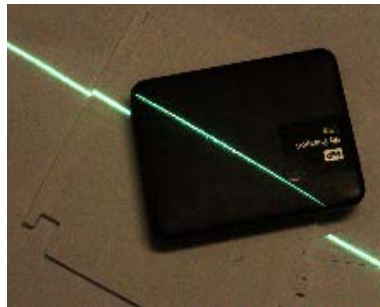


Figure 4.2 Measurement for m1 and m2.

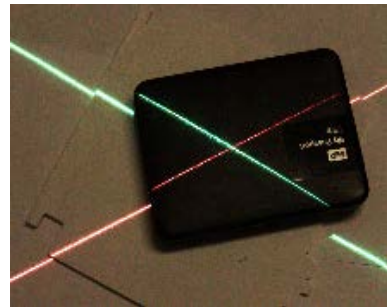
m3



a

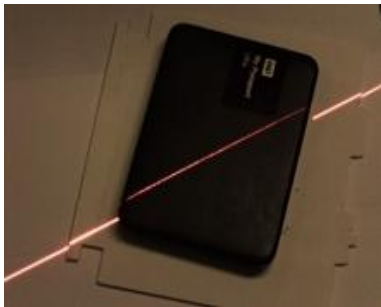


b



c

m4



a



b



c

Figure 4.3 Measurement for m3 and m4.

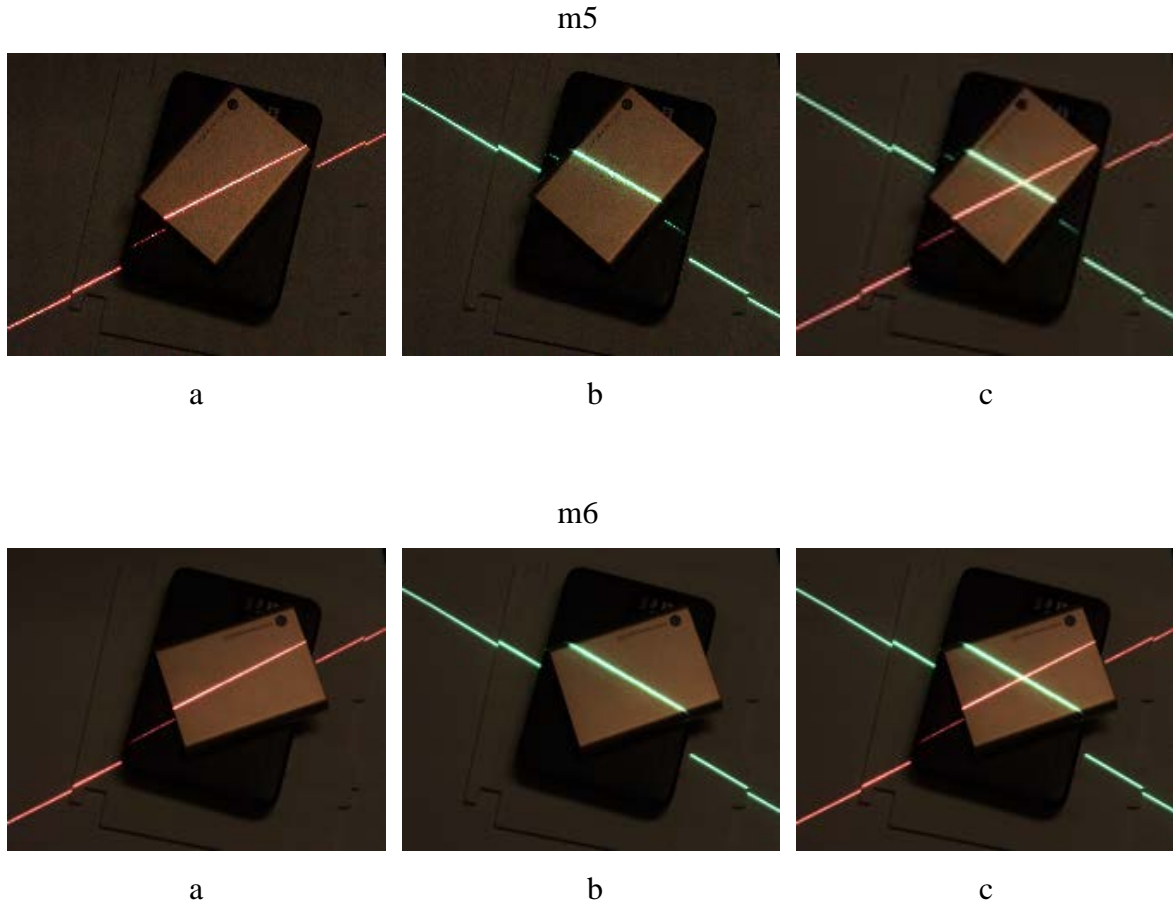


Figure 4.4 Measurement for m5 and m6

Table 4.1 Time Division Method

Measurement Number	Actual height / mm	Measure height / mm	Absolute error / mm	Relative error / %
1	10.500	11.348	0.848	8.07%
2	10.500	11.421	0.921	8.77%
3	15.748	17.199	1.451	9.22%
4	15.748	17.414	1.666	10.58%
5	26.248	28.785	2.537	9.67%
6	26.248	28.358	2.110	8.04%

As shown in Table 4.1, the actual range of Samsung SSD height measured directly by the time-division method is 11.348 ~ 11.421mm, the absolute measurement error is between 0.848

~0.921mm, while the relative error is between 8.07 ~ 8.77%. The actual range of Western SSD height measured directly is 17.199 ~ 17.414mm. The absolute measurement error is between 1.451 ~ 1.666mm, and the relative error is between 9.22 ~ 10.58%. The actual range of the height when the two are directly stacked is 28.358 ~ 28.785mm. The absolute measurement error is between 2.110~ 2.537mm, and the relative error is in a range of 8.04 ~ 9.67%.

Table 4.2 Color Division Method

Measurement Number	Actual height / mm	Measure height / mm	Absolute error / mm	Relative error / %
1	10.500	11.507	1.007	9.59%
2	10.500	11.589	1.089	10.37%
3	15.748	16.648	0.899	5.71%
4	15.748	16.784	1.036	6.58%
5	26.248	27.504	1.256	4.79%
6	26.248	27.609	1.361	5.19%

As shown in Table 2, the actual range of Samsung SSD height measured directly by the color division method is 11.507 ~ 11.589mm. The absolute measurement error is 1.007 ~ 1.089mm, and the relative error is 9.59 ~ 10.37%. The actual range of Western SSD height measured directly obtained as 16.648 ~ 16.784mm. The absolute measurement error is in a range of 0.899 ~ 1.036mm, and the relative error is between 5.71 ~ 6.58%. The actual range of the height when the two are directly stacked is achieved as 27.504 ~ 27.609mm. The absolute measurement error is in a range of 1.256 ~ 1.361mm, and the relative error is between 4.79 ~ 5.19%.

Table 4.3 Multi-level RANSAC algorithm

Measurement Number	Actual height / mm	Measure height / mm	Absolute error / mm	Relative error / %
1	10.500	11.324	0.824	7.85%
2	10.500	11.460	0.960	9.14%
3	15.748	16.839	1.091	6.93%
4	15.748	16.784	1.036	6.58%
5	26.248	27.655	1.407	5.26%
6	26.248	27.383	1.135	4.32%

As shown in Table 3, the actual range of Samsung SSD height measured directly by Multi-level RANSAC algorithm is yielded as 11.348 ~ 11.421mm. The absolute measurement error is in a range of 0.848mm ~0.960mm, and the relative error is between 7.85% ~ 9.14%. The actual range of Western SSD height measured directly is obtained as 16.784 ~ 16.839mm. The absolute measurement error is between 1.036 ~ 1.091mm, and the relative error is in a range of 6.58 ~ 6.93%. The actual range of the height when the two are directly stacked is shown as 27.383 ~ 27.655mm. The absolute measurement error is in a range of 1.135 ~ 1.407mm, and the relative error is between 4.32 ~ 5.26%.

On average, the MLRASAC algorithm has 6.70% relative error while the color division and time division offer 7.04% and 9.06%, respectively. It can be seen that the MLRANSAC algorithm offers the best results and also requires less operation time when compared with the time division and color division methods. Furthermore, there is no specific color requirement for the laser emitters. The comparison results are also depicted in Figure 4.5.

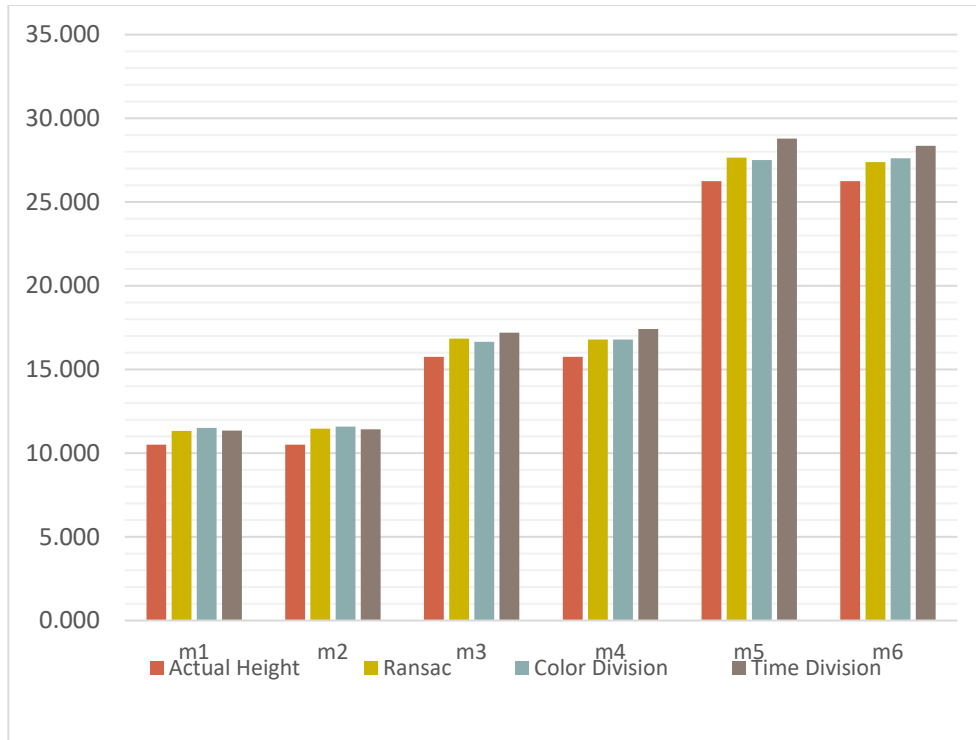


Figure 4.5 Reconstruction result

### 4.3 3-D Point Reconstruction Results

Figures 4.6-4.23 display 3-D reconstructions using each of our proposed methods. It can be seen from the following figures that the MLARANSAC algorithm has the best results

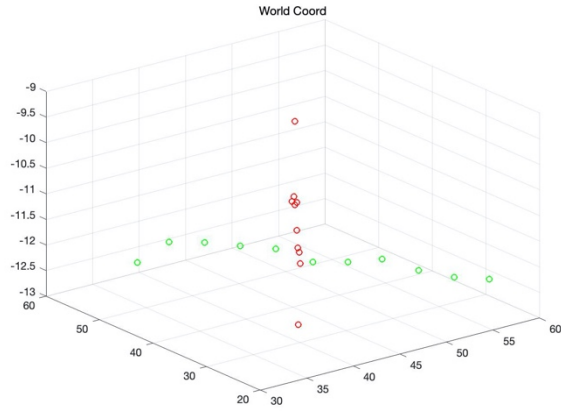


Figure 4.6 3-D reconstruction of m1 using time division.

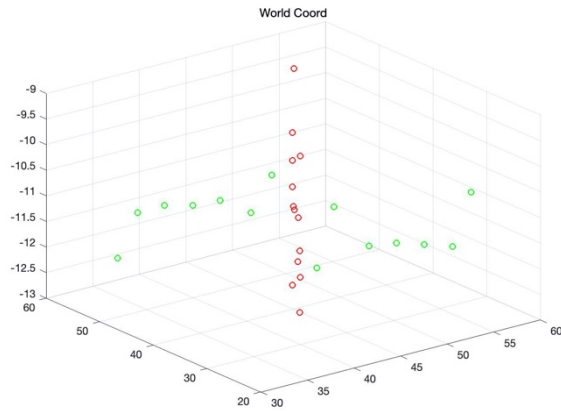


Figure 4.7 3-D reconstruction of m1 color division.

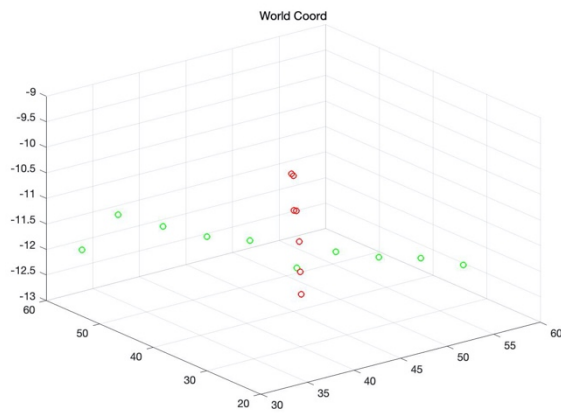


Figure 4.8 3-D reconstruction of m1 using the MLRANSAC algorithm

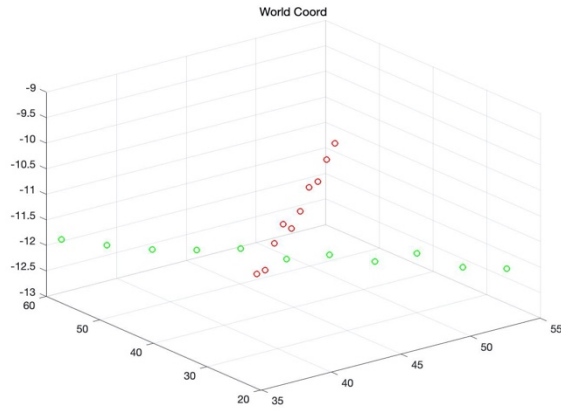


Figure 4.9 3-D reconstruction of m2 using time division.

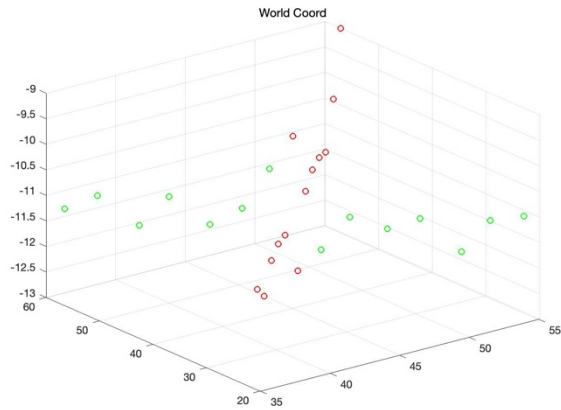


Figure 4.10 3-D reconstruction of m2 color division.

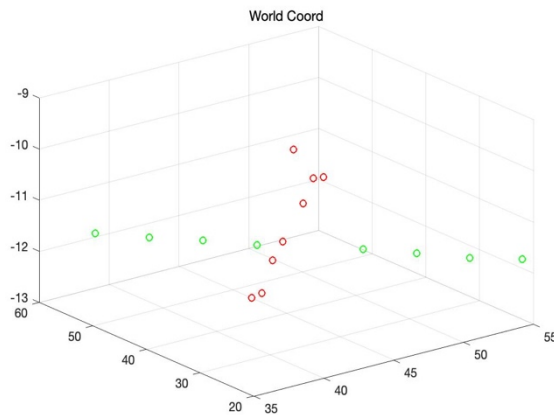


Figure 4.11 3-D reconstruction of m2 using the MLRANSAC algorithm

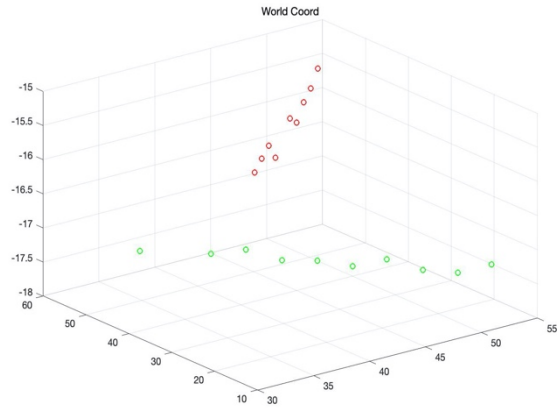


Figure 4.12 3-D reconstruction of m3 using time division.

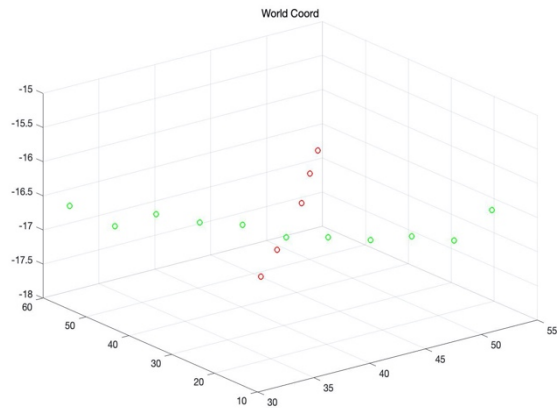


Figure 4.13 3-D reconstruction of m3 color division.

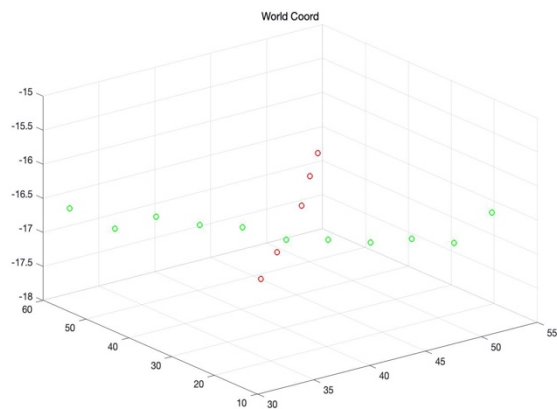


Figure 4.14 3-D reconstruction of m3 MLRANSAC algorithm

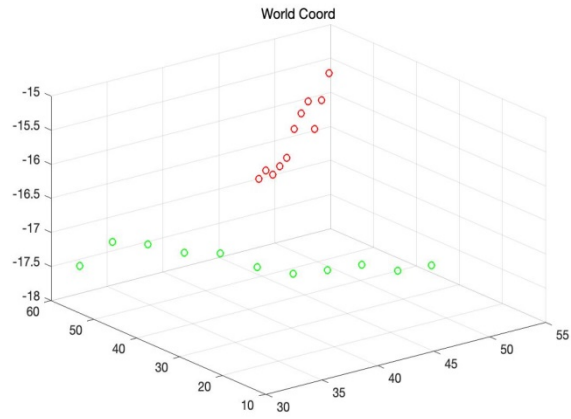


Figure 4.15 3-D reconstruction of m4 using time division.

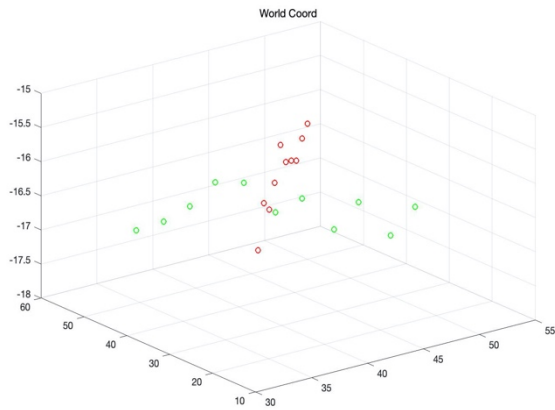


Figure 4.16 3-D reconstruction of m4 color division.

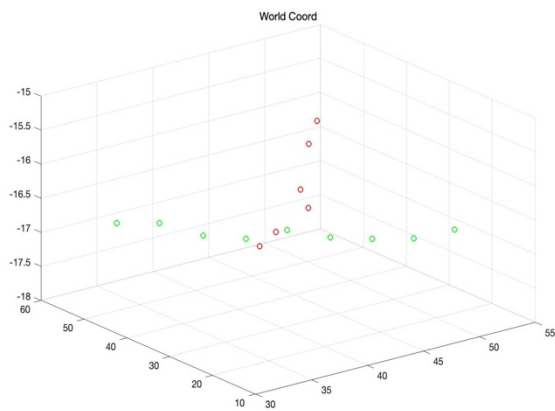


Figure 4.17 3-D reconstruction of m4 MLRANSAC algorithm

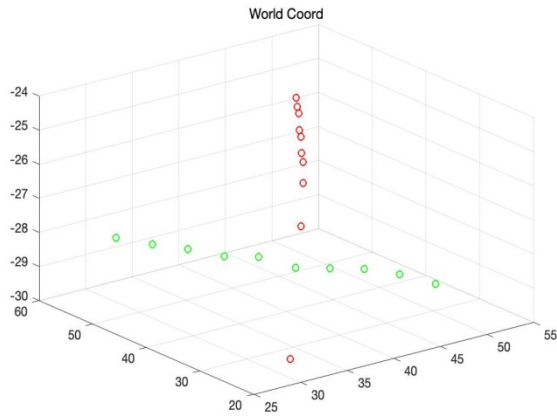


Figure 4.18 3-D reconstruction of m5 using time division.

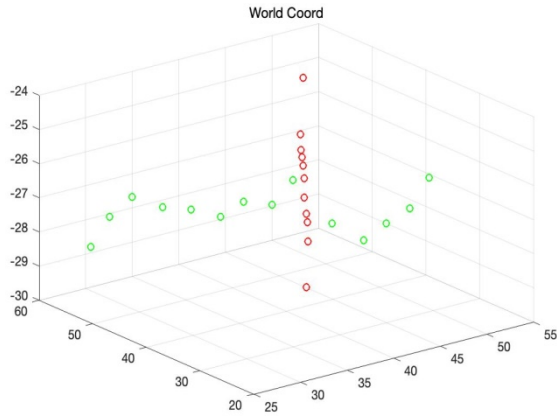


Figure 4.19 3-D reconstruction of m5 color division.

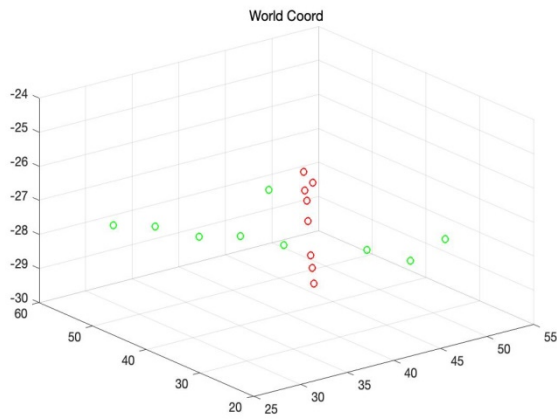


Figure 4.20 3-D reconstruction of m5 MLRANSAC algorithm

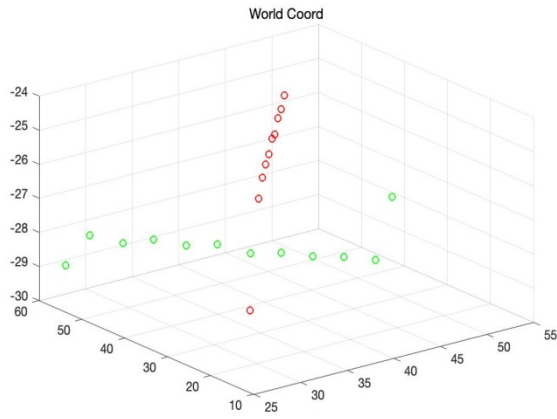


Figure 4.21 3-D reconstruction of m6 using time division.

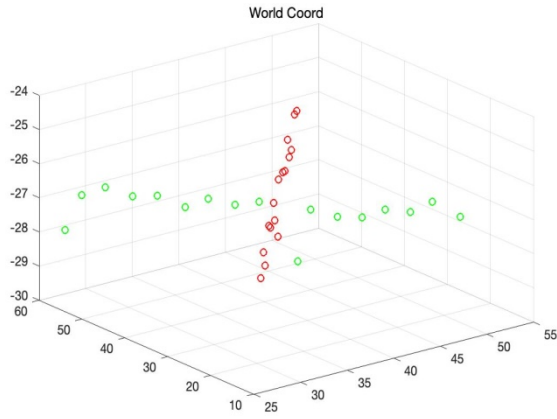


Figure 4.22 3-D reconstruction of m6 color division.

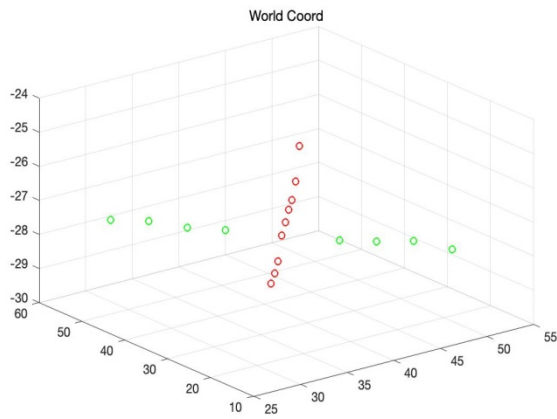


Figure 4.23 3-D reconstruction of m6 MLRANSAC algorithm

#### 4.4 Error Analysis and Engineering Suggestions

System error sources mainly include:

1. System model error: In the modeling process, errors introduced by the system model.
2. Parameter calibration error: The error introduced in the system parameter calibration process.
3. Image processing error: An error introduced during image processing.

The error of the system model mainly comes from the small hole imaging model, which can be ignored in actual measurement. The parameter calibration error primarily comes from the image processing process, such as the situation where the checkerboard corner extraction accuracy is not high when calibrating the camera parameters.

The system hardware configuration is suitable for measurement when the ambient light is weak, and the laser points can effectively fall on the measured object. Due to the limitations of the test equipment, we can only measure objects at short distances, and the size of the objects must be moderate. In actual engineering, due to the reflection of the surface of the object, the laser line shows multiple, we can adjust the light exposure rate to eliminate this effect. When the characteristics of the laser line are not distinct, the following solutions can be adopted:

1. Increase the laser power under the premise of safety.
2. Perform measurement for the condition where the ambient light is weak.

## 5. CONCLUSION

In this thesis research, we have comparatively investigated computer vision techniques for 3D reconstruction and object height measurement using a single camera and multi-laser emitters, which have an intersection on the projected image plane. The proposed time-division uses sequential operations on the laser emitters. The recommended color division method adopts the laser emitters with different colors. To improving the system, a new multi-level RANSAC (MLRANSAC) algorithm has been proposed and verified. The algorithm not only offers high accuracy for height measurement but also eliminates the different color emitter requirements. Our experiment results have validated the effectiveness of the MLRANSAC algorithm.

## REFERENCES

- [1] G. Godin et al., “Laser range imaging in archaeology: issues and results,” 2003 Conference on Computer Vision and Pattern Recognition Workshop, 2003.
- [2] H. Ha, T.-H. Oh, and I. S. Kweon, “A multi-view structured-light System for highly accurate 3D modeling,” 2015 International Conference on 3D Vision, 2015.
- [3] C. Ho, “Machine vision based 3D scanning system,” in 2009 9th International Conference on Electronic Measurement & Instruments, 2009, pp. 4-445-4-449: IEEE.
- [4] J. Li, G. Liu, and Y. Liu, “A dynamic volume measurement system with structured light vision,” in 2016 31st Youth Academic Annual Conference of Chinese Association of Automation (YAC), 2016, pp. 251-255: IEEE.
- [5] M. Garrido, M. Perez-Ruiz, C. Valero, C. Gliever, B. Hanson, and D. Slaughter, “Active optical sensors for tree stem detection and classification in nurseries,” *Sensors*, vol. 14, no. 6, pp. 10783–10803, 2014.
- [6] D. Li, H. Zhang, Z. Song, D. Man, and M. W. Jones, “An automatic laser scanning system for accurate 3d reconstruction of indoor scenes,” in 2017 IEEE International Conference on Information and Automation (ICIA), 2017, pp. 826-831: IEEE.
- [7] J. Deng, B. Chen, X. Cao, B. Yao, Z. Zhao, and J. Yu, “3D reconstruction of rotating objects based on line structured-light scanning,” in 2018 International Conference on Sensing, Diagnostics, Prognostics, and Control (SDPC), 2018, pp. 244-247: IEEE.
- [8] X. Guo, H. Zhou, G. Zhang, Y. Ke, J. Su and Z. Zhao, “Crop height measurement system based on laser vision”, *Transactions of the Chinese Society for Agricultural Machinery*, 2018.
- [9] J. Fan, F. Jing, L. Yang, L. Teng, and M. Tan, “A precise initial weld point guiding method of micro-gap weld based on structured light vision sensor,” *IEEE Sensors Journal*, vol. 19, no. 1, pp. 322-331, 2019.
- [10] S. R. Fanello et al., “HyperDepth: learning depth from structured light without matching,” presented at the 2016 IEEE Conference on Computer Vision and Pattern Recognition (CVPR), 2016.

- [11] C. Holenstein, R. Zlot, and M. Bosse, "Watertight surface reconstruction of caves from 3D laser data," 2011 IEEE/RSJ International Conference on Intelligent Robots and Systems, 2011.
- [12] X. Chen et al., "A structured-light-based panoramic depth camera," 2018 IEEE International Conference on Real-time Computing and Robotics (RCAR), 2018, pp. 102-107: IEEE.
- [13] D. Scharstein and R. Szeliski. "High-accuracy stereodepth maps using structured light," In CVPR, 2003.
- [14] M. Vo, S. G. Narasimhan, and Y. Sheikh, "Texture illumination separation for single-shot structured light reconstruction," IEEE Trans Pattern Anal Mach Intell, vol. 38, no. 2, pp. 390-404, Feb 2016.
- [15] H. Ha, T.-H. Oh, and I. S. Kweon, "A multi-view structured-light System for highly accurate 3D modeling," presented at the 2015 International Conference on 3D Vision, 2015.
- [16] L. Zhang, J. Lin, J. Sun, G. Yin, C. Ma, and L. Nie, "A robust stripe segmentation method for 3D measurement of structured light," 2015 IEEE International Conference on Mechatronics and Automation (ICMA), 2015, pp. 2431-2436: IEEE.
- [17] Bouguet, J.Y. Camera Calibration Toolbox for Matlab; California Institute of Technology: Pasadena, CA, USA, 2013.
- [18] Z. Zhang, "Flexible camera calibration by viewing a plane from unknown orientations", Proceedings of the Seventh IEEE International Conference on Computer Vision, September 1999.

## **PUBLICATIONS**

### **Conference Papers:**

Y. Zhang, Z. Lou, J. Hou, L. Tan and X. Guo, “Computer vision techniques for improving structured light vision systems,” submitted for 2020 IEEE International Conference on Electro Information Technology (EIT), Northern Illinois University, Illinois 2020.

J. Dai, Y. Zhang, J. Hou, X. Wang, L. Tan and J. Jiang, “Sparse wavelet decomposition and filter banks with CNN deep learning for speech recognition,” 2019 IEEE International Conference on Electro Information Technology (EIT), pp. 98-103, Brookings, SD, USA, 2019.